Interacting Multiscale Acoustic Vortices as Coherent Excitations in Dust Acoustic Wave Turbulence

Po-Cheng Lin and Lin I
Department of Physics and Center for Complex Systems, National Central University, Jhongli 320, Taiwan, Republic of China

(Received 16 November 2017; revised manuscript received 2 February 2018; published 28 March 2018)

In this work, using three-dimensional intermittent dust acoustic wave turbulence in a dusty plasma as a platform and multidimensional empirical mode decomposition into different-scale modes in the $2+1$D spatiotemporal space, we demonstrate the experimental observation of the interacting multiscale acoustic vortices, winding around wormlike amplitude hole filaments coinciding with defect filaments, as the basic coherent excitations for acoustic-type wave turbulence. For different decomposed modes, the self-similar rescaled stretched exponential lifetime histograms of amplitude hole filaments, and the self-similar power spectra of dust density fluctuations, indicate that similar dynamical rules are followed over a wide range of scales. In addition to the intermode acoustic vortex pair generation, propagation, or annihilation, the intra- and intermode interactions of acoustic vortices with the same or opposite helicity, their entanglement and synchronization, are found to be the key dynamical processes in acoustic wave turbulence, akin to the interacting multiscale vortices around wormlike cores observed in hydrodynamic turbulence.

DOI: 10.1103/PhysRevLett.120.135004

Turbulence is not completely disordered spatiotemporally. In hydrodynamic turbulence with a continuous power spectrum, multiscale convective vortices with worm- or filamentlike cores, appearing in the form of intermittent bursts, have been observed as the basic coherent excitations [1–4]. Strong correlations (e.g., phase synchronization and core entanglement) between different-scale vortices were also found [1–6].

Wave turbulence, which widely exists in various nonlinear media [7–13], such as water waves [7,8], optical waves [9], chemical waves [10], and acoustic waves [11,12], also exhibits a continuous power spectrum. Past studies mainly focused on the energy cascades and scaling of the continuous power spectra, multifractal and non-Gaussian dynamics, wave mixing, etc. [7–9,11–13], but to a lesser extent on the spatiotemporal waveform dynamics, especially for three-dimensional (3D) acoustic-type wave turbulence. Whether and how wave turbulence can be decomposed into different-scale coherent excitations, and their interactions, remain unexplored fundamental issues.

In the weakly disordered state before the transition to turbulence, the modulation instability for nonlinear wave systems governed by nonlinear Landau-Ginzburg or Schrödinger equations induces amplitude and phase modulations of the single-scale ordered wave. It slightly broadens the sharp peaks in the power spectrum, and generates topological defects, coinciding with amplitude holes where amplitudes are null and phases are undefined [14–20]. Moreover, in weakly disordered traveling nonlinear optical and dust acoustic waves (DAW), amplitude hole filament (AHF) pairs with opposite topological charges, winded around by helical waves with opposite helicities, named as optical vortices and acoustic vortices (AVs), respectively, were experimentally observed [14,18]. The rupture and reconnection of sequential wave crests, induced by waveform undulation of the single-scale DAW, was found to be the key for the spontaneous pair generation of AVs that can propagate in space and pairwise annihilate [18]. Namely, those AVs are the basic spontaneous coherent excitations for characterizing weakly disordered single-scale acoustic-type waveform dynamics, akin to single-scale vortex excitations in incompressible flows.

However, for wave turbulence with a continuous spectrum, the absence of spectral gaps disables spatiotemporally decomposing it into multiscale modes in the Fourier representation [3,5]. Certainly, it is intriguing to ask whether and how acoustic-type wave turbulence can be decomposed and viewed as a zoo of multiscale AVs, and how multiscale AVs are correlated spatiotemporally. In this work, by extending the acoustic vortex defect analysis of Refs. [17,18] and using a novel method, multidimensional empirical mode decomposition, these issues are experimentally tackled in the $2+1$D spatiotemporal space of the intermittent dust acoustic wave turbulence, exhibiting a continuous power spectrum with power-law decay over two decades, rather than being dominated by distinguished modes of well-defined frequencies.

The dust acoustic wave (also named dust density wave), associated with the longitudinal oscillation of negatively charged micrometer-sized dust particles in gaseous plasmas, can be self-excited through the interplay of dust inertia, screened Coulomb interactions, and ion streaming in a dusty plasma [21–23]. This fundamental nonlinear acoustic-type density wave, governed by modulation-type

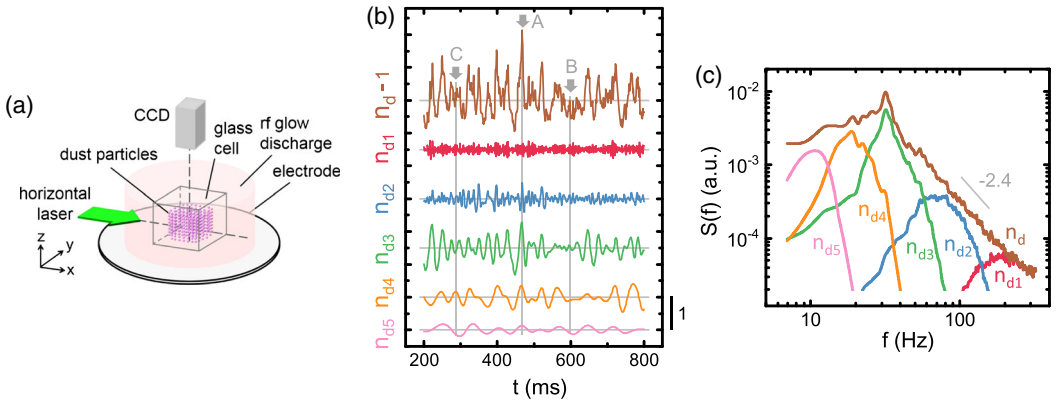

FIG. 1. (a) Sketch of the experimental system. The self-excited wave propagates downward. (b) Temporal evolution of the typical localized dust density n_d, and its decomposed n_{dj}. The gray lines indicate the zero level. Arrow A labels the example of the giant peak event in n_d, attributed to the simultaneous occurrence of the high amplitude peaks of many intrinsic mode functions (IMFs). The low amplitude regions at the troughs of the $n_d(t)$ envelope are caused by simultaneous occurrence of the low amplitude holes of some modes (e.g., at the time labeled by arrow B), or the destructive interference of some modes (e.g., at the time labeled by arrow C). (c) Corresponding power spectra of (b), with scaling exponent $= -2.4$ for the power-law decay.

nonlinear dynamical equations [21,23,24], has been used to evidence and understand generic behaviors of unstable nonlinear waves, such as defects [17–20], AHFs [17,18], rogue waves [24,25], wave turbulence [11,12], oscillons [26], and wave breaking [27]. The proper dust particle size and the spatiotemporal dynamical scales of DAW allow exploring spatiotemporal waveform dynamics in the $2+1$D space-time space through optically visualizing large-area dust density evolution illuminated by a laser sheet [17,18].

The experiment is conducted in a cylindrical radio frequency dusty plasma system, as sketched in Fig. 1(a) (see more details in Supplemental Material [28]) and also Refs. [17,18]. The self-excited intermittent turbulent wave, evidenced by the irregular waveform with large amplitude intermittent bursts and a continuous power spectrum exhibiting power-law decay over two decades, propagates downward in the $-z$ direction [Figs. 1(b), 1(c), and 2(a)]. The dust image in the xy plane illuminated by an expanded thin horizontal laser sheet is captured by a fast charge-coupled device (CCD). The normalized local dust density $n_d(x,y,t)$ can be obtained by measuring the coarse-grained image brightness I_d, normalized by its temporal average.

Through the sifting process in the empirical mode decomposition (EMD) based on Hilbert-Huang transform for a single time series, $n_d(t)$, from a local point in the xy plane, is successively decomposed in terms of adaptively obtained, amplitude-frequency modulated oscillatory IMF with zero mean, $n_{dj}(t)$ $(j=1,2,\ldots,N)$, until reaching the residue $r(t)$ describing the mean trend [6,29–31]. Namely, $n_d(t)=\sum_{j=1}^{N} n_{dj}(t)+r(t)$ and $n_{dj}=a_j(t)\cos\phi_j(t)$.

This complete and nearly orthogonal reconstruction reveals time-dependent variations of the amplitude a_j and the phase ϕ_j for mode j, with a typical timescale $\bar{\tau}_j$, the mean oscillation period of mode j. It has been widely used for characterizing nonstationary multiscale fluctuations [6,29–31], but not for spatiotemporal waveform dynamics in wave turbulence. For example, it was used to decompose the single point magnetic field time series in solar wind turbulence [6].

From temporal variable $n_d(x,y,t)$ at all local points on the xy plane, the single variable EMD is further expanded to the multidimensional EMD. For mode j, the spatiotemporal evolution of the phase and the amplitude, i.e., $\phi_j(x,y,t)$ and $a_j(x,y,t)$ obtained from $n_{dj}(x,y,t)$, are used to identify the excitations of AVs with cores along AHFs in the xyt space, and determine their helicities, which are the same as the topological charges [28].

Figures 1(b) and 1(c) show the temporal evolutions and power spectra of a typical local n_d and its decomposed IMFs. Obviously, there are strong amplitude and frequency modulations of all the IMFs, which cause the widely spread spectra of all IMFs in Fig. 1(c) and the large amplitude fluctuation of n_d in Fig. 1(b). The superposition of those widely spread IMF spectra with similar power-law dependence (IMF2 to IMF5) leads to the continuous power spectrum of n_d exhibiting a power-law decay with exponent equaling -2.4 in Fig. 1(c). Although the shapes of the modulation envelopes of IMFs of n_d look irregular, there are strong correlations between the envelopes of different IMFs. The large spikes of $n_d(t)$ (e.g., as labeled by arrow A) are from the simultaneous occurrence of the envelope peaks of several IMFs in which their peaks are also phase locked. The amplitude holes [i.e., at the troughs of the $n_d(t)$ envelope] are caused by simultaneous occurrence of the amplitude holes of some IMFs (e.g., at time labeled by arrow B) and the destructive interference of some IMFs with out-of-phase nonsmall amplitudes (e.g., at time labeled by arrow C).

Figure 2(a) shows the spatiotemporal waveform of $n_d(x,y,t)$ in the xyt space. Note that $n_d(x,y,t)$ averaged over time equals 1. Basically, the irregular waveform

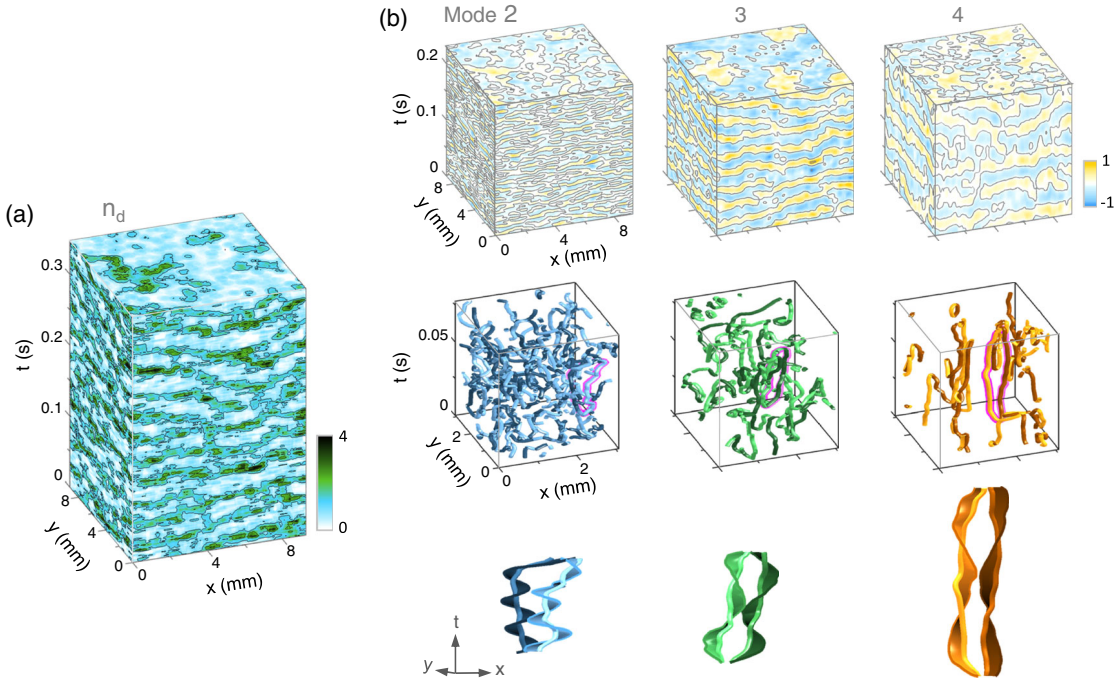

FIG. 2. (a) Color-coded plots of n_d on the xy, xt, and yt planes showing the turbulent spatiotemporal waveforms. (b) Top row: similar plots of the decomposed waveforms n_{d2}, n_{d3}, and n_{d4} of the three major modes 2 to 4 (see more details of the phase plots and the corresponding defect locations in Fig. S1 of Supplemental Material [28]). Middle row: chaotic AHFs of three major modes 2, 3, and 4 in the xyt space. The AHFs with lighter (darker) color in each panel coincide with the defect filaments with $+1$ (-1) topological charges. Bottom row: examples of waveforms showing the AVs with helical wave crest surfaces winding around the AHF pair (the thick tubes along the edges of the ribbonlike crest surfaces), zoomed up from the AHF pairs with red labeled by pink edges in the middle row. They manifest the pair generation, propagation, and pair annihilation of AVs with opposite helicities. In each row of **b**, all the panels share the same scales as those of the left panel.

exhibits strong waveform undulations. The top two rows of Fig. 2(b) further depict the waveforms of $n_{dj}(x, y, t)$ and their corresponding AHFs of major modes 2 to 4. Figure S1 of Supplemental Material [28] shows the phase $[\phi_j(x, y, t)]$ plots for modes 1 to 4, with examples labeling defect locations.

Regardless of the chaotic appearance of those AHFs in the xyt space, as shown in the middle row of Fig. 2(b), their dynamics is not completely disordered. For each mode, AHFs winded by AVs with opposite helicities can be pairwise generated and annihilated, similar to those in weakly disordered single-scale DAW [18]. As the examples show in the bottom row of Fig. 2(b), zoomed up from the AHF pairs with the pink edges in the corresponding panels of the middle row of Fig. 2(b), each AHF pair indicated by the thick filaments is winded by helical wave crests with opposite helicities. They are the silent cores of AVs. As illustrated in video 1 in Ref. [28] showing the temporal evolutions of AVs for modes 2–4, AVs in each mode can be spontaneously and pairwise generated, propagate in space, and annihilate with their twin sisters or another AV with opposite helicities from other pair generation to conserve the total topological charges (helicities). Namely, the generic behaviors of AV dynamics in weakly disordered single-scale DAW [18] can be further extended to each decomposed mode of DAW turbulence.

Figure 3(a) shows the histograms of the AV lifetime τ of different modes (see more statistical details in Ref. [28]). The larger j modes have larger spread of τ. After rescaling τ by the averaged period $\bar{\tau}_j$ of n_{dj}, the histogram of each mode obeys the similar stretched exponential decay indicated by the gray line $[P_d \propto \exp -3.6(\tau/\bar{\tau}_j)^{0.6}]$, with a descending tail starting around $\tau/\bar{\tau}_j = 1$ in the double logarithmic plot of the inset of Fig. 3(a). The increasing averaged AV lifetime with j can also be evidenced from the second row of Fig. 2(b) and video 1 in Supplemental Material [28]. The self-similar rescaled lifetime histograms and the self-similar IMF spectra [rescaled by the peak frequencies; see Fig. 1(c)] of different modes indicate that similar dynamical rules are followed over a wide range of scales.

Are there any correlations between two AVs with different combinations of mode number and helicity? Figure 3(b) shows an example of AHFs (AV cores) for modes 3 and 4 in the xyt space. Beyond their chaotic appearance, Fig. 3(c) shows the radial pair correlation functions $C(r)$ of the core locations (in the xy plane) of finding two AVs with different combination of mode number and helicity, at separation r in the xy plane (see more statistical details in [28]). Basically, for the same mode, the AVs with the opposite (same) helicity (topological charge) exhibit short range attraction (repulsion),

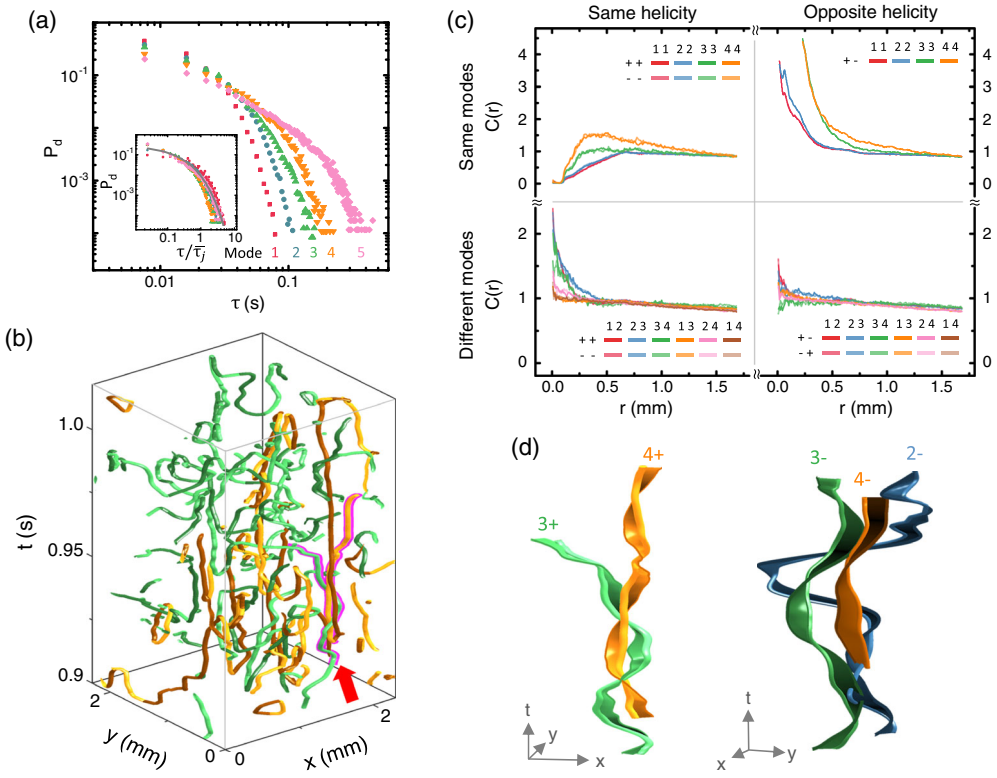

FIG. 3. (a) AV lifetime histograms of modes 1 to 5. The inset shows that, after rescaling the time by the mean period $\bar{\tau}_j$ of n_{dj}, the histogram of each mode obeys the similar stretched exponential decay indicated by the gray line [$P_d \propto \exp -3.6(\tau/\bar{\tau}_j)^{0.6}$]. (b) Plots of AHFs of the two major modes 3 and 4, with the same color codes for mode numbers and helicities as those in Fig. 2(b). (c) Radial pair correlation functions $C(r)$ of the core locations of two AVs in the xy plane with separation r and different combination of mode numbers and helicities, as indicated by the numbers and + and − symbols, respectively. (d) Two examples of the plots of AV crest surfaces winding around their AHF cores, each color coded by the mode numbers, demonstrating the temporary entanglement and bunching of two and three AVs from different modes but with the same helicity. The two AVs in the left panel of (d) are the AVs with pink edges, with the starting point indicated by the red arrow of (b).

which leads to the higher (lower) $C(r)$ in the small r regime. It implies the higher energy needed for sequential kinking and rupture of adjacent wave crest surfaces [18], to generate and separate an AV pair.

However, from different modes, two AVs with the same helicity [third quadrant of Fig. 3(c)] exhibit short range attraction, especially with the stronger attraction between AVs from adjacent modes. The tendency to approach each other can be further illustrated by the plots of the wave crest surfaces surrounding the AHFs of the two and the three AVs in Fig. 3(d), showing their temporary entanglement and bunching, respectively. When the two AVs [corresponding to the two AVs with pink edges, and starting point indicated by the red arrow in Fig. 3(b)] approach each another, they wind around each other. The entanglement lasts a short period of time, in which their phases are locked, as evidenced by the synchronized evolutions of the orientations of the AV crest surfaces in the locking period. Similar synchronization can also be found for the crest surfaces of the three AVs when they approach one another.

Note that, in hydrodynamics turbulence, the winding and merging of wormlike vortex cores with two different scales and their synchronization have also been reported [3,5]. Also note that two AVs from different modes but with opposite helicities exhibit very weak attraction [see the fourth quadrant of Fig. 3(c)], probably indirectly induced through the attraction from the third AV with the same mode number but with opposite helicity to those of any one of the two AVs. The detailed mechanisms for the observed correlation between AVs need to be further investigated.

In conclusion, through novel multidimensional EMD, we demonstrate for the first time that the 3D dust acoustic wave turbulence can be decomposed and viewed as a zoo of interacting multiscale AVs as basic spontaneous collective excitations, exhibiting attraction, repulsion, entanglement, bunching, and synchronization, in the $2+1$D spatiotemporal space. For each mode, the AV pair with opposite helicities winding around the wormlike AHF cores can be pairwise generated, propagate, and be pairwise annihilated, similarly to that in the weakly disordered single-scale DAW. AV lifetime, rescaled by the mean period of each mode, follows a common stretched exponential distribution. Two AVs with the opposite (same) helicity from the same mode exhibit short range attraction (repulsion), while

two AVs with the same helicity but different mode numbers exhibit short range attraction. The latter intermode AV attraction leads to the observed temporary entanglement or bunching of two or even three AVs with the same helicity but different mode numbers, in which their phases are locked.

Our study sheds light on decomposing and understanding the basic multiscale coherent excitations of 3D density wave turbulence in plasma and gaseous media, and 3D traveling wave turbulence in other nonlinear media.

This work is supported by the Ministry of Science and Technology, Taiwan, under Contract No. MOST-105-2112-M-008-005-MY3.

[1] Z. S. She, E. Jackson, and S. A. Orszag, Nature (London) **344**, 226 (1990).
[2] J. Jiménez, A. A. Wray, P. G. Saffman, and R. S. Rogallo, J. Fluid Mech. **255**, 65 (1993).
[3] M. Farge, G. Pellegrino, and K. C. Schneider, Phys. Rev. Lett. **87**, 054501 (2001).
[4] A. P. Finne, T. Araki, R. Blaauwgeers, V. B. Eltsov, N. N. Kopnin, M. Krusius, L. Skrbek, M. Tsubota, and G. E. Voloik, Nature (London) **424**, 1022 (2003).
[5] M. Farge, Annu. Rev. Fluid Mech. **24**, 395 (1992).
[6] S. Perri, V. Carbone, A. Vecchio, R. Bruno, H. Korth, T. H. Zurbuchen, and L. Sorriso-Valvo, Phys. Rev. Lett. **109**, 245004 (2012).
[7] E. Falcon, C. Laroche, and S. Fauve, Phys. Rev. Lett. **98**, 094503 (2007).
[8] H. Punzmann, M. G. Shats, and H. Xia, Phys. Rev. Lett. **103**, 064502 (2009).
[9] D. Pierangeli, F. DiMei, G. DiDomenico, A. J. Agranat, C. Conti, and E. DelRe, Phys. Rev. Lett. **117**, 183902 (2016).
[10] A. S. Mikhailov and K. Showalter, Phys. Rep. **425**, 79 (2006).
[11] J. Pramanik, B. M. Veeresha, G. Prasad, A. Sen, and P. K. Kaw, Phys. Lett. A **312**, 84 (2003).
[12] Y. Y. Tsai, M. C. Chang, and L. I, Phys. Rev. E **86**, 045402 (R) (2012).
[13] G. V. Kolmakov, P. V. E. McClintock, and S. V. Nazarenko, Proc. Natl. Acad. Sci. U.S.A. **111**, 4727 (2014).
[14] F. T. Arecchi, G. Giacomelli, P. L. Ramazza, and S. Residori, Phys. Rev. Lett. **67**, 3749 (1991).
[15] I. S. Aranson and L. Kramer, Rev. Mod. Phys. **74**, 99 (2002).
[16] S. Alonso, F. Sagués, and A. S. Mikhailov, Science **299**, 1722 (2003).
[17] M. C. Chang, Y. Y. Tsai, and L. I, Phys. Plasmas **20**, 083703 (2013).
[18] Y. Y. Tsai and L. I, Phys. Rev. E **90**, 013106 (2014).
[19] J. D. Williams, Phys. Rev. E **89**, 023105 (2014).
[20] K. O. Menzel, O. Arp, and A. Piel, Phys. Rev. Lett. **104**, 235002 (2010).
[21] N. N. Rao, P. K. Shukla, and M. Y. Yu, Planet. Space Sci. **38**, 543 (1990).
[22] P. Kaw and R. Singh, Phys. Rev. Lett. **79**, 423 (1997).
[23] P. K. Shukla and B. Eliasson, Rev. Mod. Phys. **81**, 25 (2009).
[24] W. M. Moslem, R. Sabry, S. K. El-Labany, and P. K. Shukla, Phys. Rev. E **84**, 066402 (2011).
[25] Y. Y. Tsai, J. Y. Tsai, and L. I, Nat. Phys. **12**, 573 (2016).
[26] S. Zhdanov, M. Schwabe, C. Rath, H. M. Thomas, and G. E. Morfill, Europhys. Lett. **110**, 35001 (2015).
[27] L. W. Teng, M. C. Chang, Y. P. Tseng, and L. I, Phys. Rev. Lett. **103**, 245005 (2009).
[28] See Supplemental Material at http://link.aps.org/supplemental/10.1103/PhysRevLett.120.135004 with video 1 and video 2. Video 1 shows spatiotemporal evolutions of amplitude hole filaments, with the brighter color and the darker color ones representing + and − helicity, respectively, for three different modes 2–4, corresponding to those shown in the second row of Fig. 2(b). Video 2 shows the spatiotemporal evolutions of amplitude hole filaments, with the brighter color and the darker color ones representing + and − helicity, respectively, for modes 3 and 4, corresponding to those shown in the second row of Fig. 3(b).
[29] N. E. Huang, Z. Shen, S. R. Long, M. C. Wu, H. H. Shih, Q. Zheng, N. C. Yen, C. C. Tung, and H. H. Liu, Proc. R. Soc. A **454**, 903 (1998).
[30] N. E. Huang and Z. Wu, Rev. Geophys. **46**, RG2006 (2008).
[31] F. Ji, Z. Wu, J. Huang, and E. P. Chassignet, Nat. Clim. Change **4**, 462 (2014).